Highlights

Molecular dynamics study of stiffness and rupture of axonal membranes

Maryam Majdolhosseini, Svein Kleiven, Alessandra Villa*

- Developing a realistic molecular model of axolemma based on experimental data about its lipid composition
- Investigating how lipid composition and protein concentration affect the membrane's structural and mechanical properties
- Identifying the most vulnerable regions of the axonal membrane

Molecular dynamics study of stiffness and rupture of axonal membranes

Maryam Majdolhosseini[a], Svein Kleiven[a], Alessandra Villa[*b]

[a]*Neuronic Engineering KTH Royal Institute of Technology Stockholm 14152 Sweden*
[b]*PDC Center for High Performance Computing KTH-Royal Institute of Technology Stockholm 11428 Sweden*

Abstract

Diffuse axonal injury (DAI), characterized by widespread damage to axons throughout the brain, represents one of the most devastating and difficult to treat forms of traumatic brain injury. Different theories exist about the mechanism of DAI, among which, one hypothesis states that membrane poration of the axons initiates DAI. To investigate the hypothesis, molecular models of axonal membranes, incorporating 25 different lipids distributed asymmetrically in the leaflets, were developed using a coarse-grain description and simulated using molecular dynamics techniques. Employing a bottom-top approach, the results were coupled with a finite element model representing the axon at the cell level. Different protein concentrations were embedded inside the lipid bilayer to describe the different sub-cellular parts in myelinated and unmyelinated axon. The models were investigated in equilibration and under deformation to characterize the structural and mechanical properties of the membranes and comparisons were made with other subcellular parts, particularly myelin. The results indicate that pore formation in the node-of-Ranvier occurs at a lower rupture strain compared to other axolemma part, whereas myelin poration exhibits the highest rupture strains among the investigated models. The observed rupture strain for the node-of-Ranvier aligns with experimental studies, indicating a threshold for injury at axonal strains exceeding 10-13% depending on the strain rate. The results indicate that the hypothesis suggesting mechanoporation triggers axonal injury cannot be dismissed, as this phenomenon occurs within the threshold of axonal injury.

Keywords: Molecular dynamics, axolemma, mechanoporation, diffuse axon injury, traumatic brain injury

1. Introduction

Traumatic brain injury (TBI) is the brain pathology caused by an external force applied to the brain in traffic or sport accidents, falls or violence [1]. Diffuse axonal injury (DAI) is a common type of TBI that affects the brain in cellular and sub-cellular levels. Mild to low-moderate DAI cannot often be diagnosed by conventional imaging techniques, though these injuries cause microscopic pathology in the brain tissue that can disrupt normal brain function [2]. Therefore,

[*]Corresponding author
Email address: avilla@kth.se (Alessandra Villa[*])

to gain more insights on the mechanism of this type of injury, it is important to use alternative techniques for investigating it in cellular and sub-cellular levels.

Swollen and disconnected axons are indicative of DAI at the cellular level [3, 4]. Axons are elongated projections of nerve cells. They can be myelinated or un-myelinated. Myelinated axons are wrapped by a multi-layer sheath called myelin. Myelin does not cover the whole axon and gaps between myelin sheaths are called node-of-Ranvier. Fig. 1 provides a schematic representation of a neural cell together with a sub-cellular representation of axonal membranes.

Experimental studies showed that the lipid composition of membranes in different cells and subcellular elements varies significantly and affects the function and properties of the cells (Table 1) [5]. Various studies have investigated how lipid content and cholesterol concentration affect the mechanical and structural properties of lipid bilayers [6, 7, 8, 9, 10, 11, 12]. These studies have highlighted the significant impact of molecular composition on membrane properties such as area compressibility [6, 7, 8, 9, 11], but also the effect on processes like mechanoporation [9, 10, 11, 12], interdigitation [10, 8], and bilayer thinning [7, 12] in non-equilibrium states. The high dependence of bilayer properties on lipid composition emphasizes the necessity for an accurate and specific molecular model that captures the unique composition of the axolemma. Such a model would enable a more comprehensive investigation of the axolemma's properties and behavior under deformation.

Table 1: Lipid composition (weight fraction) of different membranes. For experimental data, the mean weight fraction is provided along with its corresponding standard deviation. Lipid head-groups are abbreviated as follows: phosphatidylcholine (PC), phosphatidylethanolamine (PE), sphingomyelin (SM), phosphatidylserine (PS), cholesterol (CHOL)

	PC	PE	SM	PS	Glycolipid	CHOL	Other
Experimental composition (% weight)							
Axolemma [13, 14, 15]	21 ± 5	20 ± 5	3 ± 4	4 ± 2	20 ± 12	24 ± 3	4 ± 2
Myelin [16]	11 ± 1	17 ± 1	6 ± 3	6 ± 1	28 ± 3	28 ± 1	4 ± 2
Brain white matter [17]	12 ± 1	20 ± 2	-	9 ± 1	24 ± 5	27 ± 6	9 ± 2
MD models composition (% weight)							
Axolemma model	22	23	3	4	15	29	5
Myelin model [11]	12	22	3	9	23	29	2
Plasma membrane model [18]	30	17	17	6	5	17	8

Axonal membrane or axolemma contains many membrane proteins, acting as ion channels and transporters, which play a vital role in the physiological functioning of cells. The concentration of these proteins is not uniform along the axon. This variation has been shown to affect how the axonal membrane reacts during an impact [19, 20].

As shown in Fig. 1, the node-of-Ranvier exhibits a higher concentration of ion channel proteins in the membrane, while unmyelinated axons have on average a lower ion-channel concentration. Among the proteins that exist in the axolemma, we find voltage-gated sodium channels as one of the most abundant ones in the brain and axonal cells. Among this class of protein, Nav1.1 proteins are particularly prevalent in axon initial segments and the node-of-Ranvier [21, 22].

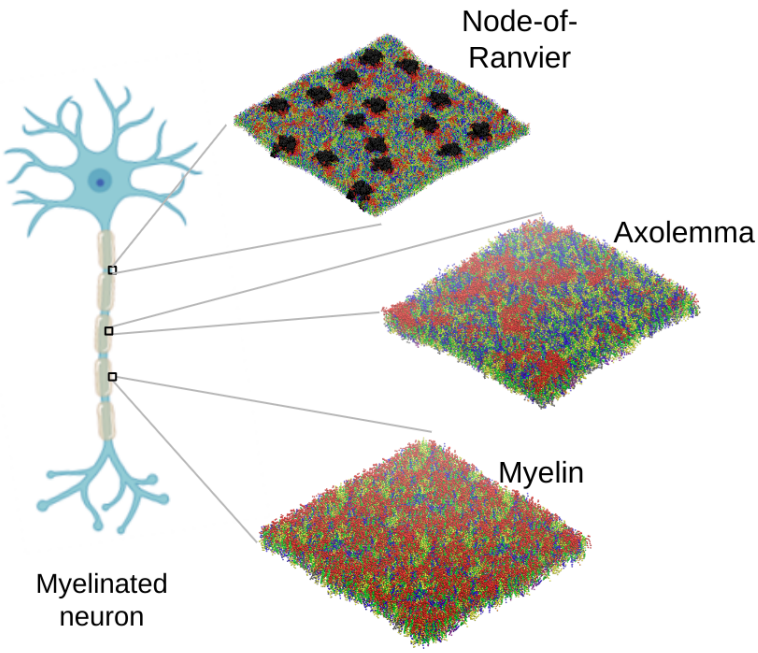

Fig. 1: A schematic view of a myelinated neuron together with snapshot of the simulated bilayers. The arrow connect the bilayers to the corresponding element in the neural cell. Axolemma and the node-of-Ranvier have the same lipid composition. Lipids are illustrated as follows: PC lipids are in blue, PE in yellow, SM in orange, PS in purple, glycolipids in red and CHOL in green. The proteins are represented in black. Water and ions are not shown. For abbreviations see 1

Investigations of injuries at the cellular level usually employ techniques such as atomic force microscopy [23], micropipette aspiration [24, 25], laser-induced cavitation [26, 27], transient pressurised fluid deflection [28], cell culture deformation [29], and computational modelings [30, 31]. However, capturing sub-cellular mechanisms of injuries and data on local strains and stresses from experiments is challenging due to their time and length scales that are in order of nanoseconds and nanometers. Alternatively, to get more detailed data modeling techniques at different levels like finite element (FE) modeling and molecular dynamics (MD) simulations can be used to study brain injuries and elucidating their mechanisms at sub-cellular and molecular levels [32, 33].

Studies investigating the axonal injury in sub-cellular level have lead to multiple hypotheses about the initial trigger of injury. One hypothesis regarding the primary mechanism of

axonal injury is mechanoporation, which involves the formation of pores in the axonal membrane [34, 35, 36, 10, 37, 38]. Another proposed hypothesis is cytoskeletal damage of the axon [23, 39]. However, computational studies utilizing FE models of the axon, incorporating major cytoskeletal components and the axonal membrane, have rejected the hypothesis that damage to microtubules triggers axonal injury[36]. These FE studies have demonstrated high levels of strain primarily on the axonal membrane rather than the microtubules, suggesting that the membrane is more susceptible to injury than this cytoskeletal element.

On molecular level, different models are developed in-situ to investigate the properties of membranes from different brain cells [10, 11, 9, 40]. For example, Ingolfsson et al. provided a generalized membrane model for the brain [40] and Saeedimasine et al. developed a model to describe the myelin sheath [11].

Here, we aim to gain a better understanding of whether the mechanoporation of axonal membranes can trigger axonal injury using molecular modelling. To achieve this, we first-of-all need to develop a model that accurately describes the axolemma composition. Then using molecular dynamics techniques, we can tackle which sub-cellular compartment of the axon undergoes poration first and how lipid composition and protein concentration affect mechanical properties of membranes. For this purpose, we have developed a coarse grained (CG) model of axolemma based on experimental data. To elucidate the effect of the protein in the membrane, we embed different concentrations of protein inside the bilayer. In total, we derived three models representing different parts of the axon. The models were simulated in equilibrium and under deformation. Finally, to simulate an injury condition, the systems were subjected to uniaxial deformation. According to the hypothesis, membrane poration was considered as the time when axonal damage initiated. Therefore, in the last step, we combined the deformation results in molecular simulations with the equivalent deformation of axolemma in an FE model of an axon in cellular level under uniaxial tension [41].

2. Calculations

2.1. Molecular model for axon

Axolemma is described as a bilayer consisting of different types of lipids distributed asymmetrically in the extracellular and cytoplasmic leaflet of the axon cells. We developed the model utilizing existing experimental data on the lipid composition of the axolemma, their distribution within the extracellular and cytoplasmic leaflets, and their saturation index [14, 42, 40, 11]. Lipid composition and distribution between leaflets, saturation index, and tail length were determined using a combination of experimental data and information from established brain-type membrane models. While overall lipid composition of axolemma, fatty acid composition and unsaturation index of PC and PE were derived from experiments on human brain reported by DeVries et al. [14], neuron data reported by Fitzner et al. was used to derive chain length and saturation number in PS [42]. In case the experimental data on axolemma were missing, information on more general brain-type membrane models were used [40, 11]. Namely, lipid disposition in the extracellular and cytoplasmic leaflet was derived from the brain membrane model developed by Ingólfsson et al. [40].

The cryo-EM structure of human Nav1.1, as presented by Pan et al. [43], available in the protein data bank (PDB ID: 7DTD), was utilized to describe the protein system. Three distinct models for the axon membrane were created with varying protein concentrations within the membrane to mimic the membrane in different sections of the axon. Experimentally the density of sodium channels in the axonal membrane differs across regions, ranging from 5 to 3000

$channels/\mu m^2$, with the highest concentration found at the node-of-Ranvier [44, 45, 46]. One model is without protein, called "Axolemma" model, one with only 1 embedded protein ("one-protein-axolemma") and one with 16 embedded proteins, with equivalent protein concentration of 2519 $channels/\mu m^2$, labelled as "node-of-Ranvier".

2.2. System setup

All the molecules were described at the coarse-grained (CG) level using Martini 2.2 force field [47]. The starting structure of the membrane without the protein was built using INSANE (INSert membrANE) bilayer builder [48] and Martinizer python code was employed to transform the protein's all-atom structure into a coarse-grained model [49]. The protein's overall shape was constrained using the ElNeDyn approach [50], to control the overall conformation of the protein.

A bilayer was first built using 1004 lipids and 820 cholesterol solvated by 52177 water beads, with 0.15 mol concentration of Na-Cl as ions in a box of size $20 \times 20 \times 20$ nm^3. Then equilibration run was performed for the lipids to find their most suited neighboring configuration. The equilibrated system was then used to build a larger system $38 \times 38 \times 24$ nm^3. This system was equilibrated under the same condition for 20 microseconds, before deformation.

In order to simulate the node-of-Ranvier, a larger concentration of proteins were embedded inside the membrane according the following procedure. First, one protein was embedded in an equilibrated axonal membrane model of size $20 \times 20 \times 20$ nm^3 and the system was equilibrated again. Then, a larger system with a box size of $80 \times 80 \times 20$ nm^3 containing 16 proteins was developed from a previously equilibrated model, representing a system with protein concentration of 2519 $channels/\mu m^2$.

2.3. Molecular dynamics simulation

All the simulations were performed in the GROMACS simulation package[51], version 2020 and 2021 [52, 53]. After energy minimization, all the systems were equilibrated at NPT condition. The pressure and temperature were kept constant at 1 bar using C-rescale barostat [54] ($\tau_p = 12.0\ ps$, $\kappa = 3 \times 10^{-4}\ bar^{-1}$) and at 310 K using V-rescale thermostat [55] ($\tau_T = 1.0\ ps$), respectively. The time-step was 10 fs with Verlet cut-off scheme for non-bonded interactions that were updated every 20 steps with cutoff radius of 1.1 nm for both Coulomb and van der Waals interactions. Long-range interactions were defined using reaction field. The models containing proteins were first equilibrated by having position restraints on the proteins to relax lipid distribution around the protein and then, the position restraint on the proteins were removed to allow the proteins to move freely as well. For the one-protein-axolemma, the protein-lipid contacts and energy of the system did not change much after removing the position restraint of the protein (supplementary Fig. S 1); therefore, the last frame of the system with restrain on the protein was used to run the deformation simulations. However, the proteins in the node-of-Ranvier model tend to move when they are free, so the deformation is applied to the system after being equilibrated for 11 μs with no position restraint. Table 3 and supplementary Table S2 provides the information about how different systems were developed and simulated in more detail.

To explore pore formation under strain, we initially deformed the systems with rate of 1×10^{-5} nm/ps in the x-direction until 30% of deformation. We then conducted two subsequent deformations with slower rates of 1×10^{-6} nm/ps and 1×10^{-7} nm/ps on the deformed model. This allowed us to observe and analyze the impact of deformation rate on pore formation. All the simulations were run for at least 3 times. In order to compare the properties of the developed systems with myelin model by Saeedimasine et. al, similar deformation runs were also applied to the equilibrated model for the myelin.

All the simulations were conducted on the Dardel supercomputer, where each compute node is equipped with two AMD EPYC™ Zen2 2.25 GHz 64-core processors, offering a total of 128 physical CPU cores per node. For example, a single node achieves a performance of 1000 ns/day for the axolemma system (approximately 300,000 particles). This means that, on average, we require 10,400 CPU hours (54 days) to obtain results for each of the four molecular systems, from equilibration to pore formation. Consequently, this amounts to more than 5.4 million CPU hours of simulation time across all cores.

2.4. Equilibrium and mechanical properties

2.4.1. System in equilibration

In order to check the equilibration of the system and the lipid aggregation in equilibrium, enrichment factor was calculated and compared for the last 10 μs of equilibrium for each lipid type based on the method proposed by Corradi et al. [56]:

$$Enrichment factor\,(L) = \frac{Ratio\,(L)_x}{Ratio\,(L)_{bulk}} \tag{1}$$

In which: $Ratio\,(L)_x = \frac{no.\,(L)_x}{(total\ no.\ lipids)_x}$, is calculated by dividing the number of type L lipids within the distance of x from the given lipid by total number of lipids within the distance of x from the given lipid and $Ratio\,(L)_{bulk} = \frac{total\ no.\ L}{total\ no.\ lipids}$, is defined as the total number of type L lipids in the system divided by total number of lipids.

For the systems with protein, we use $Ratio\,(L)_x$ to define the protein neighboring. The cut-off distance was set to be 1.5 and 2.1 nm to calculate lipid-lipid enrichment factor in axolemma model and protein-lipid neighboring in one-protein-axolemma and the node-of-Ranvier, respectively, in line with the distance chosen by Saeedimasine et al. [11].

2.4.2. System under deformation

To derive the mechanical properties of the systems, such as Young's modulus, principal stress in x direction, σ_x, and strain, ϵ_x, values were calculated as follows:

$$\sigma_x = P_{xx} \tag{2}$$

$$\epsilon_x = \frac{(x - x_0)}{x_0} \tag{3}$$

where P_{xx} is the lateral pressure in the x direction, the same direction from which the system is deformed [57], x is the bilayer dimension in x direction at different deformation points and x_0 is defined as the x dimension of the bilayer when the average surface tension of the system is zero.

The stress-strain curve of a material under deformation acts differently at different stages of deformation. At small strains, called the elastic region, there is a linear relationship between stress and strain curve and the slope of the line in this part is representative of the stiffness or Young's modulus of the system. The strain in which the stress-strain curve becomes non-linear depends on the system and its mechanical properties. The elastic region for the simulated systems in this study was until the deformation of 15%. Equation 4 shows how the Young's modulus is calculated in the elastic region.

$$Young's\ modulus = \frac{\partial \sigma_x}{\partial \varepsilon_x} \tag{4}$$

in which σ_x is the uniaxial stress, and ε_x is the strain of the system. The Young's modulus for the systems is derived from the stress-strain curve of the systems under deformation with the strain rate of 1×10^{-5} nm/ps by employing the ordinary least squares regression method in Python to fit a line to the strain-stress curves and the slope of the line along with the standard error of the fit are presented.

Another mechanical property of the bilayer is the area compressibility modulus, K_A, which is defined as the derivative of the surface tension γ with respect to areal strain ε_A at constant temperature, experimentally [58, 59].

$$K_A = \frac{\partial \gamma}{\partial \varepsilon_A} \tag{5}$$

Assuming that the surface area of the bilayer is equal to the surface area of the box, the areal strain was derived by dividing the area of the box at different deformations to the initial area of the box at strain of zero (ϵ_0). $\epsilon_A = \frac{(x \times y - x_0 \times y_0)}{(x_0 \times y_0)}$. Surface tension can also be calculated as:

$$\gamma = l_z(P_{zz} - \frac{P_{xx}}{2} - \frac{P_{yy}}{2}) \tag{6}$$

in which P_{xx}, P_{yy} are the lateral pressure, P_{zz} is the normal pressure and l_z is the height of the box.

At small deformations, there is a linear relationship between surface tension and areal strain and consequently, area compressibility modulus is constant. Therefore, to calculate this parameter, we simulated the systems in constant pressure and areal strain condition, NP_zAT, in small areal strains of up to 4.5% for 6 μs and using the data of the last 4 μs of simulations to make sure the system is in equilibrium, the production data was processed every 1 μs and the average surface tension, γ, and strain values were used to calculate the area compressibility modulus to make the results more comparable with experimental data. K_A is calculated the same regression method used to calculate the Young's modulus.

Bilayer rupture occurs with formation of a pore in the bilayer and corresponds to a sudden decrease of the surface tension and the strain at this point is considered as the rupture strain, ϵ_{pore}.

3. Results and discussion

3.1. Equilibration and structure

The axolemma is described as a bilayer consisting of 26 lipid types and cholesterol(CHOL), distributed asymmetrically in the extracellular and cytoplasmic leaflet of the axon cells. The bilayer composition (% mol) is 17% phosphatidylcholine (PC), 18% phosphatidylethanolamine (PE), 3% phosphatidylserine (PS), 4% phosphatidylinositol(PI), 2% sphingomyelin (SM), 17% glycolipids and 45% CHOL. The weight and mol fractions are reported in Table 1 together with experimental values. The specific lipid types used in developing the model along with their mole percentage in each leaflet are provided in supplementary Table S1. The extracellular leaflet primarily consisted of 20% PC, 3% SM, 21% glycolipids, 44% CHOL and 1% other lipids , while the cytoplasmic leaflet contained 14% PC, 26% PE, 5% PS, 7% PI, 46% CHOL and 2% other lipids in % mol. The developed model had a lipid composition in the range of the reported experimental values, except for a slightly higher weight fraction of CHOL in the model compared to the experimental values.

The axolemma differs in lipid composition compared to an average plasma membrane, but also other membranes in the brain. In general, it has high weight fraction of CHOL followed by PC and PE phospholipids. A high CHOL content in the axolemma is expected since membranes of the brain cells are usually more enriched in CHOL compared with other cell membranes in the body [60, 61]. The axolemma model is more enriched in PC lipids, less in glycolipids and CHOL than the myelin and average brain white matter membranes[11, 40]. In comparison with models of plasma membrane, axolemma has higher content of glycolipids while the average plasma membrane model is more enriched in PC and SM.

Tail length and saturation index also differ in different membrane models. Tail length in all the models varies between 16 to 26. While axolemma and plasma membrane models have around 80% of short tail lengths of 16-18 in both extracellular and cytoplasmic leaflets, this value is 48% for myelin in cytoplasmic leaflet and 95% in the extracellular leaflet. This difference in the tail length between the models and the leaflets for the myelin can contribute to its mechanical properties. Saturation index is also different in the models and between leaflets. While the axolemma model has unsaturation index (saturated tails/unsaturated tails) of 0.47 and 0.42 in extracellular and cytoplasmic leaflets, respectively, these values are 0.66 and 0.68 for plasma membrane model and 0.44 and 0.34 for the myelin.

To describe the axonal membranes, we use 3 models: axolemma, one-protein-axolemma and node-of-Ranvier (see section 2.1 of methods for details). All the models were equilibrated and analysed in normal physiological conditions and under deformation to mimic an accidental TBI. To check the convergence of the simulations, total energy and surface area of the bilayers were calculated over time. Both properties reached equilibrium within the first 10 μs for all models (supplementary Fig. S 2). In addition, lipid distribution in the bilayer in the axolemma model was checked and compared with the small axolemma system in the last 10 microseconds by calculating the lipid neighboring. We assumed that the system has reached equilibrium when the average number of lipid neighboring along with the surface area of the bilayer and energy of the system converged (see supplementary Fig. S 3).

During the production run and under physiological conditions, lipid distribution was investigated for the developed models and enrichment factor for each lipid type was calculated. The results shown in Fig. 2 suggest that the distribution of lipids inside the membranes is not uniform; however all models follow the same trend of lipid aggregation and depletion regardless if a protein is embedded inside or not. While phospholipids in the extracellular leaflet tend to aggregate with each other, they tend to deplete the glycolipids. The same trend can be seen for glycolipids that aggregate most with each other. In the cytoplasmic leaflet where no glycolipid exists, lipids are distributed more uniformly; however, the PS lipids tend to deplete each other. In the presence of proteins, the aggregation of glycolipids decreases in the extracellular leaflet. This change may be attributed to the fact that these lipids aggregate more with proteins, and as a consequence, the total lipids in their neighboring decreases. In the cytoplasmic leaflet, SM lipids tend to aggregate more with other lipids in the one-protein-axolemma compared to the axolemma and the node-of-Ranvier models. However, as the number of SM lipids in the system is not much (only 2% of the composition), this change will not affect the properties of the system. Comparing the results with other models, it can be seen that the model of an average brain membrane developed by Ingolfsson et al. [40] also has similar trend in the extracellular leaflet where the glycolipids co-localize and other lipids tend to aggregate with each other and deplete the glycolipids. Similar behavior can be seen for the glycolipids in the model of the plasma membrane [18], but in this model, other lipids also aggregate with glycolipids and less localization of the glycolipids can be seen. In the cytoplasmic leaflet, the distribution of lipids in the plasma membrane and brain

membrane models [18, 40] are similar to the axolemma; however, the depletion of PS lipids is not seen in these models.

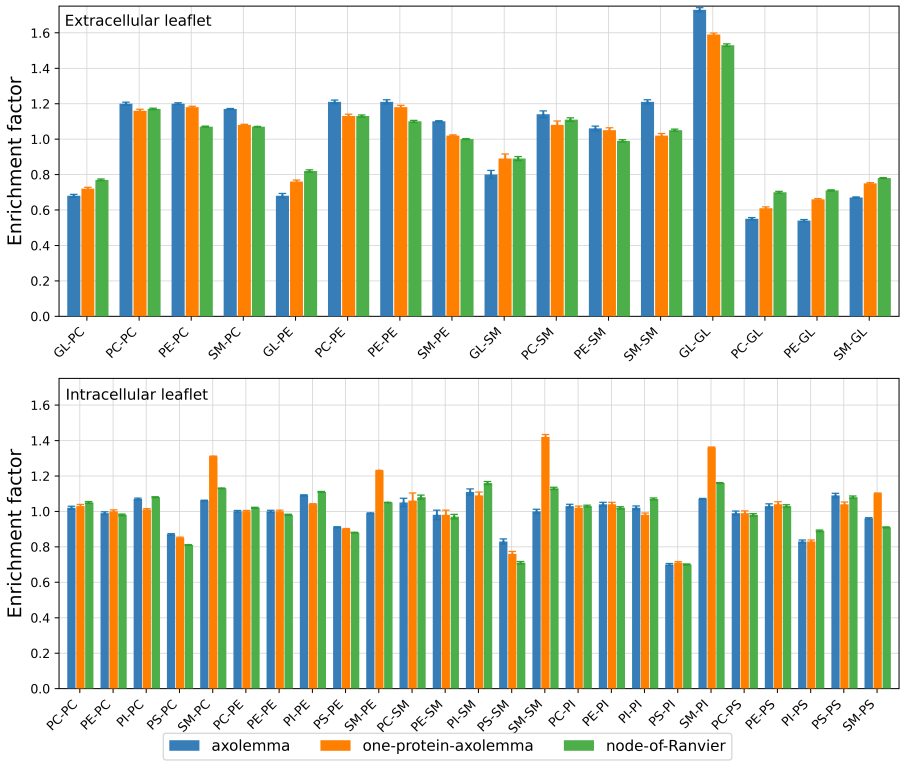

Fig. 2: Average Lipid-Lipid enrichment of different systems in the last 10 μs of equilibration along with their standard deviation shown as error-bars. For abbreviations see 1

For one-protein-axolemma model and the node-of-Ranvier, the lipid neighboring around the proteins were also calculated and the results are presented in the Table 2. From the lipid-protein aggregation data in this table, it is indicated that in both systems, about half of the lipids surrounding the protein are glycolipids in the extracellular leaflet, while SM lipids tend to be depleted from the proteins. In the cytoplasmic leaflet where no glycolipid is present, PE phospholipids are more aggregated around the protein while SM lipids deplete from the protein. Aggregation of glycolipids in the extracellular leaflet and PE phospholipids in the cytoplasmic leaflet along with SM depletion are also reported by Saeedimasine et al. [11] for the neighboring of two different plasma membrane models with different protein concentrations.

3.2. Deformation

To investigate the behaviour of the models during injury, the bilayers were deformed at different strain rates in x direction (Table 3 and supplementary Table S2). First, the system was deformed until 30% with a rate of 1×10^{-5} nm/ps and then, two subsequent deformations with slower rates of 1×10^{-6} nm/ps and 1×10^{-7} nm/ps were applied to the deformed model. Based

Table 2: Protein-lipid neighboring for the axolemma model with protein and the node-of-Ranvier at the last 10 μs of equilibrium.

	Extracellular leaflet				Cytoplasmic leaflet				
System	PC	PE	SM	GL	PC	PE	SM	PI	PS
one-protein-axolemma	0.25	0.15	0.02	0.57	0.19	0.49	0.01	0.13	0.18
node-of-Ranvier	0.27	0.18	0.04	0.51	0.21	0.47	0.02	0.14	0.16

on the results, calculated stiffness of the bilayer, rupture strain and other mechanical properties of the bilayer under deformation are reported in this section.

The values of Young's modulus representing the stiffness of the bilayers are reported in Table 4 and the stress strain points used for the fitting are plotted in Fig. 3. This value can give us more insight about the effect of protein concentration and lipid composition on the resistance of the bilayer against an applied force and deformation. The results show that all the models with axolemma composition have similar stiffness of 15-16 MPa, while the myelin model has higher stiffness (26 MPa). This suggests that the protein concentration has little effect on the stiffness of the system and this value is largely influenced by the lipid composition. We also calculated the Young's modulus of each system using strain-stress curves calculated from simulations performed at constant areal strains. The calculated stiffness values are 16.1, 14.9, 7.1 and 25.1 MPa for axolemma, one-protein-axolemma, node-of-Ranvier and myelin, respectively. While all the values are close to those derived from the stress-strain curve of the system under deformation, the Young's modulus derived for node-of-Ranvier is twice lower when calculated using the latter approach. The difference is because all systems show a stiffening behaviour by increase of the strain. Although all models reach the reported stiffness at around 5% strain, the stiffness of the node-of-Ranvier increases further and reaches the reported value at the strain of 12%.

A direct comparison between our results and experiments is not possible, as to the best of our knowledge, no experimental data has measured value of the Young's modulus for the axonal membranes under uniaxial deformation. Nevertheless, we try to compare the results with stiffness of other lipid bilayers. Jaing et al. performed tensile tests on two different silicone bilayers [62] and stress-strain data until 200% were reported. We calculated the Young's modulus of the membranes based on the reported data for the first 15% of deformation using linear regression method and derived the stiffness of 30 ± 1 and 37 ± 2 MPa for these bilayers. Other studies applying compression to lipid bilayers using atomistic force microscopy calculate a Young's modulus of 19.3 to 28.1 MPa for a bilayer of DOPC/DPPC lipids [63], 27 to 31 MPa for POPC and PDPC bilayers [64] and 50 MPa for artificial lipid bilayers of DPhPC lipids [65]. The calculated Young's modulus in the current study are in the corridor of the data derived for other membranes and lipid bilayers.

Another mechanical parameter representing the response of the bilayer area under tension is the areal compressibility modulus, K_A. This value was calculated for the systems at three different areal strain values of 0.1 to 4.5%. The reason for investigating the system under small deformations is that at higher strains, the surface tension will not grow linearly with strain while the areal compressibility modulus is defined as the linear relationship between these values. The average surface tension along with standard errors in each μs is plotted as a function of areal strain in Fig. 4 and the results for the calculated areal compressibility modulus and the

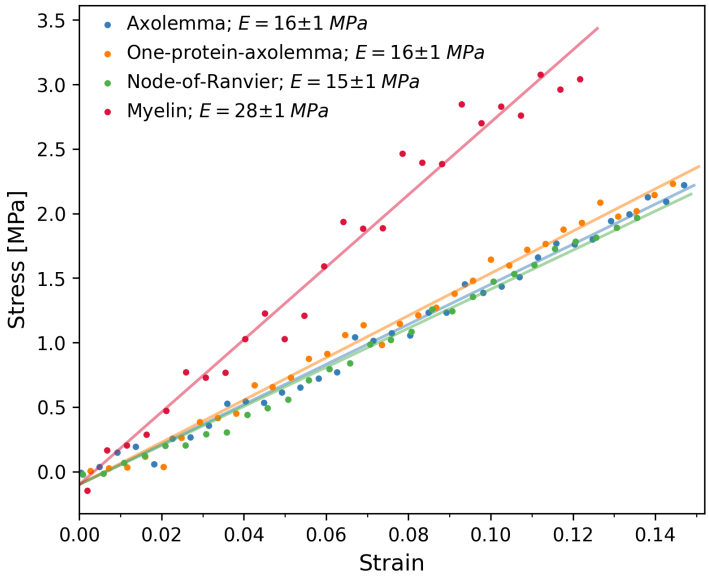

Fig. 3: Strain Stress points of the systems in the elastic part of deformation (first 15% strain) and the corresponding fitted line using linear regression method. Stress value for each system at 15% strain representing the yield stress is shown by Stars.

corresponding standard error are reported in Table 4. Despite the Young's modulus that was quite similar for all the developed models of axolemma, K_A is affected by the concentration of proteins, as the node-of-Ranvier has almost half the compressibility modulus of the axolemma model with protein. Similar results were reported in previous studies on the model of plasma membrane [11]. The myelin has the highest compressiblity modulus compared to other systems. The reported experimental values for K_A are from 179 to 450 mN/m for red blood cell membrane at 25 °C [58, 66, 67] which are in the range of values reported in this study. However, no experimental data is available for the area compressibility modulus of axonal membranes.

Table 3: Information on performed molecular dynamics simulations

Model Name	Dimension (nm)	No. of Nav1.1 proteins	Equilibration time (μs)	No. of replicas at each deformation rate (nm$\frac{ps}{s}$)		
				10^{-5}	10^{-6}	10^{-7}
Axolemma (small)	$20 \times 20 \times 20$	0	25	No deformation		
Axolemma	$38 \times 38 \times 24$	0	20	1	3	3
One-protein-axolemma	$46 \times 38 \times 19$	1	30^a	1	3	3
Node-of-Ranvier	$80 \times 80 \times 20$	16	$15^a + 11.5$	1	3	3

^{a}: simulation performed by applying position restraint on the protein

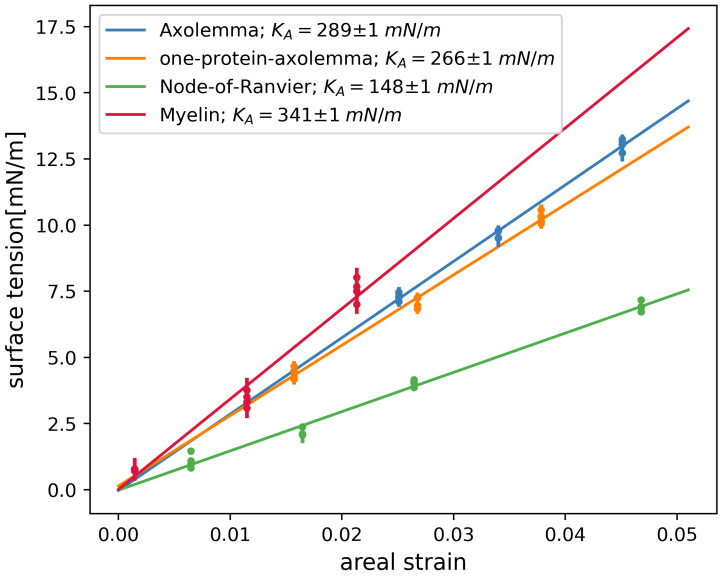

Fig. 4: Values of surface tension (mN/m) and the corresponding areal strain of different systems. Data is reported as the average and standard error of the surface tension vs. areal strain in time windows of 1 μs for each system when equilibrated in constant areal strain. Areal compressibility modulus of the systems is calculated as the slope of the line fitted to the data.

Assuming that the axonal injury is triggered by the pore formation of the axolemma, we deformed the systems until rupture at two different strain rates of 1×10^{-6} nm/ps and 1×10^{-7} nm/ps. The rupture corresponds with formation of a pore in the bilayer that will lead to a jump in the surface tension. Therefore, by monitoring the surface tension, the rupture can be detected. Strain in which the rupture occurs depends on both the molecular system and the deformation rate. Table 4 displays the mean rupture strain and standard deviation across various replicas for each system at different deformation rates. The node-of-Ranvier model exhibits a lower rupture strain compared to other systems. The results suggest a direct relationship between Young's modulus and rupture strain; however, further data and studies are needed to confirm this reliably. Additionally, as the deformation rate decreases, the rupture strain also decreases. Investigation of the pores in the membranes reveals that they form predominantly in areas with a higher concentration of PE lipids. In the one-protein-axolemma and node-of-Ranvier models, some PC lipids are also present around the pores. Notably, no glycolipids are found in the vicinity of the pores in any of the models.

Comparing the results of mechanoporation in the node-of-Ranvier with experimental studies is not possible. But a similar MD study on a plasma membrane system with similar concentration of proteins has been performed by Saeedimasine et al [11] using the MARTINI force-field and deformed in x direction with a rate of $2.5 \times 10^{-6} nm/ps$. The results suggest a strain rupture of 0.36, which is 22% lower than the strain rupture of the node-of-Ranvier. The difference stems from the differences in the lipid composition, the tail length and saturation level of the lipids. The difference in rupture strain reveals how structural properties affects the mechanical responses of membranes.

Table 4: Mechanical properties of different systems under deformation, the average rupture strain and surface tension $0.1\mu s$ before the pore for different tests are provided along with their standard error.

Model	Rupture strain	Average surface tension before pore (mN/m)	Average stress before pore (MPa)	Young's modulus (MPa)	K_A (mN/m)
Axolemma	0.51 ± 0.02^b; 0.43 ± 0.03^c	73.1 ± 0.5^b ; 70.1 ± 0.6^c	5.63 ± 0.04^b; 5.05 ± 0.03^c	15.5 ± 0.99^a	289 ± 7
One-protein-axolemma	0.50 ± 0.01^b; 0.45 ± 0.01^c	73.5 ± 0.4^b ; 71.4 ± 0.4^c	5.56 ± 0.03^b; 5.19 ± 0.03^c	16.4 ± 0.99^a	266 ± 8
Node-of-Ranvier	0.44 ± 0.01^b; 0.41 ± 0.01^c	72.3 ± 0.2^b ; 70.2 ± 0.2^c	4.84 ± 0.02^b; 4.60 ± 0.02^c	15.3 ± 0.99^a	148 ± 10
Myelin	0.53 ± 0.07^b; 0.53 ± 0.04^c	76.8 ± 0.78^b ; 77.5 ± 0.32^c	8.19 ± 0.05^b; 8.24 ± 0.04^c	26.3 ± 0.97^a	341 ± 17

* Data calculated at different deformation rates of: a: 10^{-5}; b : 10^{-6}; c : 10^{-7} nm/ps

d: Model derived from [11]

The average tension and its standard deviation at $0.1; \mu s$ before pore formation are calculated for each system. Additionally, the failure stress, which corresponds to the average stress just before pore formation, is computed at $0.1; \mu s$ before pore formation. This value represents the ultimate stress in the membrane, providing information about the maximum stress each system can endure before rupturing.

Notably, the average surface tension before pore formation remains relatively similar for the axolemma models, both with and without proteins, across various strain rates. However, the average stress before pore formation increases proportionally with the rupture strain. The reported values for myelin surpass those for axolemma models, due to myelin's higher stiffness, higher K_A, and higher rupture strain.

So far, the molecular dynamics results of the mechanical properties of different membrane systems are reported. Specifically, we investigated the areal compressibility modulus and stiffness of the systems and strain in which the membrane rupture occurs along with surface tension and ultimate stress in different deformation rates. In the next part, we couple the MD results with an FE model of the axon to calculate the axon strain in which the axonal injury might occur. We use the results of the slowest deformation rate for the systems when coupling with FE results. The deformation rate of 1×10^{-7} nm/ps correspond to strain rate of 3000 s^{-1} for axolemma, one-protein-axolemma and myelin models and 1500 s^{-1} for the node-of-Ranvier. It is crucial to note that the rates mentioned here are 30 to 300 times faster than the strain rates observed in experimental studies on brain tissue damage and real-world scenarios [68]. This notable difference arises from the inherently high computational cost and time associated with each simulation.

3.3. Multi-scale coupling

To investigate the membrane poration and how it leads to axonal damage at cellular level, we have coupled the molecular results with a generic FE model of the axon under stretch. The FE axon model was previously developed by Montanino and Kleiven and described in details in Ref[36]. Briefly, the axon is modeled as an 8 μm cylinder consisting of microtubules, neurofilaments and tau proteins connecting the fibers together and an axolemma-cortex compartment surrounding the whole model. To minimize the effect of microtubule discontinuity on axonal behavior, 5 different axonal models with different microtubule discontinuity locations were stretched. Subsequently, the axon undergoes deformation under uniaxial strain at varying rates.

The strain applied to the axon leads to non-uniform deformation across its sub-cellular components. Employing a bottom-up approach, we assume that each element of the cortex corresponds to the membrane systems developed at the molecular level. Therefore, the deformation observed at the MD scale corresponds to the local strain experienced by each element of the cortex in the FE model. Fig. 5 shows how the FE and MD models are coupled together.

Fig. 5: Coupling FE model of the axon in cellular level with molecular systems representing the axonal membrane [10]. a) FE model of the undeformed axon in cellular level; A quarter of the axon model is removed for better representation of the sub-cellular elements. b) A single element on the cortex in an undeformed state corresponding with the membrane models in molecular level. c) Undeformed lipid bilayer of the axolemma with one embedded protein. d) FE model of the axon under uniaxial deformation in cellular level. e) The cortex element with the maximum local strain during the axonal deformation is extracted. f) Lipid bilayer of the axolemma with one embedded protein undergoing the maximum local strains of the cortex element (figure adapted and modified from [10]).

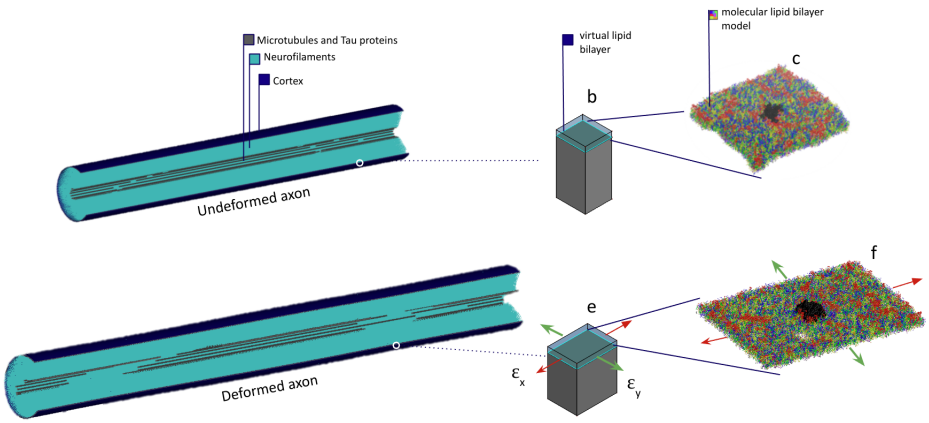

To calculate the axonal strain at which membrane poration occurs, we identified the cortex element with the highest local strain and analyzed the obtained total axonal strain. Fig. 6 illustrates the maximum local strain within the cortex in the FE model, alongside the corresponding axonal strain under various strain rates. Furthermore, the strain in which the mechanoporation occurs in MD is marked with the corresponding membrane. The node-of-Ranvier has a rupture strain of 41% which corresponds to axonal strain of 9.8 to 13.2 % depending on the strain rate, while the myelin seems to form rupture at higher strains compared to other membranes.

A direct comparison of the results with available experimental data is not possible as the threshold for axonal injury in the brain is difficult to define precisely due to the complex nature of TBI [69]. Moreover, the specific threshold for axonal strain in the brain is influenced by various

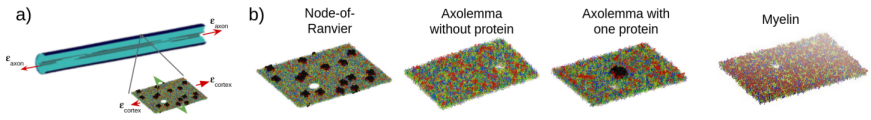

maximum axolemma strain (ε_{cortex})	0.41	0.43	0.45	0.55
$\varepsilon_{axon}(\dot{\varepsilon} = 1\ s^{-1})$	13.2%	14%	14.5%	17.6%
$\varepsilon_{axon}(\dot{\varepsilon} = 10\ s^{-1})$	9.8%	10.2%	10.5%	12%
$\varepsilon_{axon}(\dot{\varepsilon} = 20\ s^{-1})$	10%	10.2%	10.5%	11.5%
$\varepsilon_{axon}(\dot{\varepsilon} = 40\ s^{-1})$	12%	12.1%	12.3%	13.4%

Fig. 6: Coupling the molecular dynamics results with finite element model of the axon under deformation. a) A schematic view of deformation in axon that leads to mechanoporation of the membrane and axonal injury. b) Axonal strain with the corresponding element with maximum local strain for different deformation rates are provided in the table and the strain in which each system undergoes mechanoporation is marked.

factors, including the location of the injury, the direction and magnitude of the forces applied, and the individual characteristics of the brain tissue. However, experiments using animal models and computational studies have provided some insights into the biomechanical thresholds associated with axonal injury. For example, animal studies have shown that strains ranging from 10% to 20% can lead to axonal injury in the brain [69]. In another study on the neurons of rat embryo it was shown that strains more than 10% would result in total break of axonal bundles [29]. Another study that applyed 10% lagrangian strain with the rate of 20 /s to organotypic hippocampal slice cultures showed a moderate brain damage that was detected 4 days after the injury but not 2 days after the injury [70]. In contrast to our results, an experiment on the guinea pig optic nerve done by Bain and Meaney, the range of critical strain for axonal damage was shown to be between 0.14 to 0.34 with strain rate of 30 to 60 /s, below which no nerve was injured [71]. This difference might be due to mechanical differences between animal and human axons, or due to the fact that the axon model that is used in this study is isolated, while it is shown that the axons can withstand larger strains when embedded inside the tissue [41].

It is essential to recognize certain limitations within this study. First, the deformation rate of the MD models is considerably faster than that of typical injury events, resulting in a rate mismatch. However, due to the high computational cost of MD simulations, it was not feasible to run the deformations at a slower rate. Additionally, we used a CG model, which allows for simulations with larger time steps and thus enables slower deformation rates. In addition, we could not compare the results directly with experiments, as there is no experiment specifically performed on axonal membranes and their behavior under deformation. But our findings still were in line with previous studies on deriving mechanical properties of other membranes and bilayers. Moreover, coupling the results with FE studies show that the rupture strain is in line with reported thresholds of axonal injuries in experimental studies.

4. Conclusion

This study aimed to illuminate the mechanism of axonal injury, specifically focusing on the possible role of the membrane poration under strain. For this purpose, a molecular model

of the axolemma was developed, taking into account its lipid composition and tail information derived from experimental data. Models with different protein concentrations were considered to replicate different regions of the axon. The developed models along with myelin developed by Saeedimasine et al. [11] were deformed until rupture and the mechanical properties were compared. Our findings revealed that among axonal membranes, myelin exhibited the highest stiffness and also had a greater rupture strain and stress at the point of pore formation. In contrast, the node-of-Ranvier had the lowest rupture strain and stiffness and counted as the most vulnerable part of the axonal membrane. However, the tension and stress at the pore were not significantly different for the models of the axonal membrane, suggesting that these parameters are primarily influenced by the lipid composition of the membrane rather than the protein concentration.

We then combined the MD simulation results with a FE model of the axon to get more understanding of the mechanism of the axonal injury and its initial trigger and shed light to the behaviour of sub-cellular elements of the axons during an impact. We get the rupture strain for each membrane model from MD and the axonal strain at which local membrane mechanoporation occurs from FE simulations and then compared the injury threshold with experimental findings. The simulation results indicate that the mechanoporation of the membrane occurs in the range of 10 to 13 % of axonal strain which aligns with the experimental data and therefore supports the hypothesis stating that mechanoporation might trigger axonal injury. In addition, the study highlights how combining FE and MD approaches can explore complex multi-scale phenomena that cannot be investigated by a single method.

Author contributions

Maryam Majdolhosseini: Methodology, Validation, Formal analysis, Data Curation, Investigation, Resources, Visualization, Writing – original draft. **Svein Kleiven:** Supervision, Resources, Writing – review and editing, Funding acquisition. **Alessandra Villa:** Conceptualization, Methodology, Supervision, Resources, Writing – review and editing, Funding acquisition.

Declaration of Competing Interest

The authors declare no conflict of interest.

Acknowledgements

The computational resources were provided by the National Academic Infrastructure for Supercomputing in Sweden (NAISS) through Center for High Performance Computing (PDC) at KTH under Projects NAISS 2024/22-601, SNIC 2021/5-459, SNIC 2022/5-645, and SNIC 2021/5-406. We would like to acknowledge Jing Gong and Johan Hellsvik at the KTH PDC Center for their assistance with the installation of the necessary software on the PDC resources.

Funding

This study was supported by research funds from Swedish Research Council Grants VR-2020-04496.

References

[1] G. T. Manley, A. I. R. Maas, Traumatic brain injury: an international knowledge-based approach, Jama 310 (5) (2013) 473–474.

[2] S. S. Humble, L. D. Wilson, L. Wang, D. A. Long, M. A. Smith, J. C. Siktberg, M. F. Mirhoseini, A. Bhatia, S. Pruthi, M. A. Day, others, Prognosis of diffuse axonal injury with traumatic brain injury, The journal of trauma and acute care surgery 85 (1) (2018) 155.

[3] M. E. Komlosh, D. Benjamini, E. B. Hutchinson, S. King, M. Haber, A. V. Avram, L. A. Holtzclaw, A. Desai, C. Pierpaoli, P. J. Basser, Using double pulsed-field gradient MRI to study tissue microstructure in traumatic brain injury (TBI), Microporous and Mesoporous Materials 269 (2018) 156–159.

[4] D. H. Smith, D. F. Meaney, W. H. Shull, Diffuse axonal injury in head trauma, The Journal of head trauma rehabilitation 18 (4) (2003) 307–316.

[5] T. Harayama, H. Riezman, Understanding the diversity of membrane lipid composition, Nature Reviews Molecular Cell Biology 19 (2018) 281.
URL `https://doi.org/10.1038/nrm.2017.138 http://10.0.4.14/nrm.2017.138`

[6] W. Jiang, Y. C. Lin, Y. L. Luo, Mechanical properties of anionic asymmetric bilayers from atomistic simulations, Journal of Chemical Physics 154 (22) (2021). doi:10.1063/5.0048232.

[7] A. Rasouli, Y. Jamali, E. Tajkhorshid, O. Bavi, H. N. Pishkenari, Mechanical properties of ester- and ether-DPhPC bilayers: A molecular dynamics study, Journal of the Mechanical Behavior of Biomedical Materials 117 (2021). doi:10.1016/j.jmbbm.2021.104386.

[8] D. Drabik, G. Chodaczek, S. Kraszewski, M. Langner, Mechanical Properties Determination of DMPC, DPPC, DSPC, and HSPC Solid-Ordered Bilayers, Langmuir 36 (14) (2020). doi:10.1021/acs.langmuir.0c00475.

[9] M. Saeedimasine, A. Montanino, S. Kleiven, A. Villa, Role of lipid composition on the structural and mechanical features of axonal membranes: a molecular simulation study, Scientific reports 9 (1) (2019) 1–12.

[10] A. Montanino, M. Saeedimasine, A. Villa, S. Kleiven, Localized axolemma deformations suggest mechanoporation as axonal injury trigger, Frontiers in neurology 11 (2020) 25.

[11] M. Saeedimasine, A. Montanino, S. Kleiven, A. Villa, Elucidating axonal injuries through molecular modelling of myelin sheaths and nodes of Ranvier, Frontiers in Molecular Biosciences 8 (2021) 669897.

[12] M. C. Oliveira, M. Yusupov, A. Bogaerts, R. M. Cordeiro, Molecular dynamics simulations of mechanical stress on oxidized membranes, Biophysical Chemistry 254 (2019) 106266.

[13] G. H. DeVries, C. J. Zmachinski, The Lipid Composition of Rat CNS Axolemma-enriched Fractions, Journal of Neurochemistry 34 (2) (1980). doi:10.1111/j.1471-4159.1980.tb06613.x.

[14] G. H. DeVries, W. J. Zetusky, C. Zmachinski, V. P. Calabrese, Lipid composition of axolemma-enriched fractions from human brains., Journal of lipid research 22 (2) (1981) 208–216.

[15] G. H. DeVries, W. Payne, R. G. Saul, Composition of axolemma-enriched fractions isolated from bovine CNS myelinated axons, Neurochemical Research 6 (5) (1981). doi:10.1007/BF00964391.

[16] M. N. Rasband, W. B. Macklin, J. A. Benjamins, Myelin Structure and Biochemistry, Basic Neurochemistry: Principles of Molecular, Cellular, and Medical Neurobiology: Eighth Edition (2012) 180–199doi:10.1016/B978-0-12-374947-5.00010-9.

[17] N. U. Olsson, A. J. Harding, C. Harper, N. Salem, High-performance liquid chromatography method with light-scattering detection for measurements of lipid class composition: Analysis of brains from alcoholics, Journal of Chromatography B: Biomedical Applications 681 (2) (1996). doi:10.1016/0378-4347(95)00576-5.

[18] H. I. Ingólfsson, M. N. Melo, F. J. van Eerden, C. Arnarez, C. A. Lopez, T. A. Wassenaar, X. Periole, A. H. de Vries, D. P. Tieleman, S. J. Marrink, Lipid Organization of the Plasma Membrane, Journal of the American Chemical Society 136 (41) (2014) 14554–14559. doi:10.1021/ja507832e.
URL `https://doi.org/10.1021/ja507832e`

[19] B. Hille, Ionic channels in excitable membranes. Current problems and biophysical approaches, Biophysical journal 22 (2) (1978) 283–294.

[20] J. S. Trimmer, K. J. Rhodes, Localization of voltage-gated ion channels in mammalian brain, Annu. Rev. Physiol. 66 (2004) 477–519.

[21] I. Ogiwara, H. Miyamoto, N. Morita, N. Atapour, E. Mazaki, I. Inoue, T. Takeuchi, S. Itohara, Y. Yanagawa, K. Obata, others, Nav1. 1 localizes to axons of parvalbumin-positive inhibitory interneurons: a circuit basis for epileptic seizures in mice carrying an Scn1a gene mutation, Journal of Neuroscience 27 (22) (2007) 5903–5914.

[22] A. Duflocq, B. Le Bras, E. Bullier, F. Couraud, M. Davenne, Nav1. 1 is predominantly expressed in nodes of Ranvier and axon initial segments, Molecular and Cellular Neuroscience 39 (2) (2008) 180–192.

[23] M. H. Magdesian, F. S. Sanchez, M. Lopez, P. Thostrup, N. Durisic, W. Belkaid, D. Liazoghli, P. Grütter, D. R. Colman, Atomic force microscopy reveals important differences in axonal resistance to injury, Biophysical Journal 103 (3) (2012). doi:10.1016/j.bpj.2012.07.003.

[24] Y. Wu, T. Cheng, Q. Chen, B. Gao, A. G. Stewart, P. V. Lee, On-chip surface acoustic wave and micropipette aspiration techniques to assess cell elastic properties, Biomicrofluidics 14 (1) (2020). doi:10.1063/1.5138662.
[25] E. Ibarboure, M. Fauquignon, J. F. Le Meins, Obtention of giant unilamellar hybrid vesicles by electroformation and measurement of their mechanical properties by micropipette aspiration, Journal of Visualized Experiments 2020 (155) (2019). doi:10.3791/60199.
[26] A. N. Hellman, B. Vahidi, H. J. Kim, W. Mismar, O. Steward, N. L. Jeon, V. Venugopalan, Examination of axonal injury and regeneration in micropatterned neuronal culture using pulsed laser microbeam dissection, Lab on a Chip 10 (16) (2010). doi:10.1039/b927153h.
[27] A. Selfridge, D. Preece, V. Gomez, L. Z. Shi, M. W. Berns, A model for traumatic brain injury using laser induced shockwaves, in: K. Dholakia, G. C. Spalding (Eds.), Optical Trapping and Optical Micromanipulation XII, Vol. 9548, SPIE, 2015, p. 95480P. doi:10.1117/12.2189724.
URL https://doi.org/10.1117/12.2189724
[28] R. S. Chung, J. A. Staal, G. H. McCormack, T. C. Dickson, M. A. Cozens, J. A. Chuckowree, M. C. Quilty, J. C. Vickers, Mild axonal stretch injury in vitro induces a progressive series of neurofilament alterations ultimately leading to delayed axotomy, Journal of Neurotrauma 22 (10) (2005). doi:10.1089/neu.2005.22.1081.
[29] Y. Li, C. Li, C. Gan, K. Zhao, J. Chen, J. Song, T. Lei, A precise, controllable in vitro model for diffuse axonal injury through uniaxial stretch injury, Frontiers in Neuroscience 13 (OCT) (2019). doi:10.3389/fnins.2019.01063.
[30] R. J. Cloots, J. A. Van Dommelen, T. Nyberg, S. Kleiven, M. G. Geers, Micromechanics of diffuse axonal injury: Influence of axonal orientation and anisotropy, Biomechanics and Modeling in Mechanobiology 10 (3) (2011). doi:10.1007/s10237-010-0243-5.
[31] M. Kazempour, M. Baniassadi, H. Shahsavari, Y. Remond, M. Baghani, Homogenization of heterogeneous brain tissue under quasi-static loading: a visco-hyperelastic model of a 3D RVE, Biomechanics and Modeling in Mechanobiology 18 (4) (2019). doi:10.1007/s10237-019-01124-6.
[32] A. T. N. Vo, M. A. Murphy, P. K. Phan, T. W. Stone, R. K. Prabhu, Molecular dynamics simulation of membrane systems in the context of traumatic brain injury, Current Opinion in Biomedical Engineering (2023) 100453.
[33] M. F. Horstemeyer, R. K. Prabhu, Multiscale Biomechanical Modeling of the Brain, Academic Press, 2021.
[34] D. K. Cullen, V. N. Vernekar, M. C. LaPlaca, Trauma-induced plasmalemma disruptions in three-dimensional neural cultures are dependent on strain modality and rate, Journal of neurotrauma 28 (11) (2011) 2219–2233.
[35] M. C. LaPlaca, V. M.-Y. LEE, L. E. Thibault, An in vitro model of traumatic neuronal injury: loading rate-dependent changes in acute cytosolic calcium and lactate dehydrogenase release, Journal of neurotrauma 14 (6) (1997) 355–368.
[36] A. Montanino, S. Kleiven, Utilizing a structural mechanics approach to assess the primary effects of injury loads onto the axon and its components, Frontiers in neurology 9 (2018) 643.
[37] M. C. LaPlaca, M. C. Lessing, G. R. Prado, R. Zhou, C. C. Tate, D. Geddes-Klein, D. F. Meaney, L. Zhang, Mechanoporation is a potential indicator of tissue strain and subsequent degeneration following experimental traumatic brain injury, Clinical Biomechanics 64 (2019) 2–13.
[38] E. H. PETTUS, C. W. CHRISTMAN, M. L. GIEBEL, J. T. POVLISHOCK, Traumatically induced altered membrane permeability: its relationship to traumatically induced reactive axonal change, Journal of neurotrauma 11 (5) (1994) 507–522.
[39] M. D. Tang-Schomer, V. E. Johnson, P. W. Baas, W. Stewart, D. H. Smith, Partial interruption of axonal transport due to microtubule breakage accounts for the formation of periodic varicosities after traumatic axonal injury, Experimental Neurology 233 (1) (2012). doi:10.1016/j.expneurol.2011.10.030.
[40] H. I. Ingólfsson, T. S. Carpenter, H. Bhatia, P.-T. Bremer, S. J. Marrink, F. C. Lightstone, Computational lipidomics of the neuronal plasma membrane, Biophysical journal 113 (10) (2017) 2271–2280.
[41] A. Montanino, M. Saeedimasine, A. Villa, S. Kleiven, Axons embedded in a tissue may withstand larger deformations than isolated axons before mechanoporation occurs, Journal of biomechanical engineering 141 (12) (2019).
[42] D. Fitzner, J. M. Bader, H. Penkert, C. G. Bergner, M. Su, M.-T. Weil, M. A. Surma, M. Mann, C. Klose, M. Simons, Cell-type-and brain-region-resolved mouse brain lipidome, Cell reports 32 (11) (2020) 108132.
[43] X. Pan, Z. Li, X. Jin, Y. Zhao, G. Huang, X. Huang, Z. Shen, Y. Cao, M. Dong, J. Lei, others, Comparative structural analysis of human Nav1. 1 and Nav1. 5 reveals mutational hotspots for sodium channelopathies, Proceedings of the National Academy of Sciences 118 (11) (2021) e2100066118.
[44] H. Hu, P. Jonas, A supercritical density of Na+ channels ensures fast signaling in GABAergic interneuron axons, Nature neuroscience 17 (5) (2014) 686–693.
[45] J. Ritchie, R. B. Rogart, Density of sodium channels in mammalian myelinated nerve fibers and nature of the axonal membrane under the myelin sheath., Proceedings of the National Academy of Sciences 74 (1) (1977) 211–215.
[46] K. T. Wann, Neuronal sodium and potassium channels: structure and function, BJA: British Journal of Anaesthesia 71 (1) (1993) 2–14.
[47] S. J. Marrink, H. J. Risselada, S. Yefimov, D. P. Tieleman, A. H. De Vries, The MARTINI force field: coarse grained model for biomolecular simulations, The journal of physical chemistry B 111 (27) (2007) 7812–7824.

[48] T. A. Wassenaar, H. I. Ingólfsson, R. A. Bockmann, D. P. Tieleman, S. J. Marrink, Computational lipidomics with insane: a versatile tool for generating custom membranes for molecular simulations, Journal of chemical theory and computation 11 (5) (2015) 2144–2155.

[49] D. H. de Jong, G. Singh, W. F. D. Bennett, C. Arnarez, T. A. Wassenaar, L. V. Schafer, X. Periole, D. P. Tieleman, S. J. Marrink, Improved parameters for the martini coarse-grained protein force field, Journal of chemical theory and computation 9 (1) (2013) 687–697.

[50] X. Periole, M. Cavalli, S. J. Marrink, M. A. Ceruso, Combining an elastic network with a coarse-grained molecular force field: Structure, dynamics, and intermolecular recognition, Journal of Chemical Theory and Computation 5 (9) (2009). doi:10.1021/ct9002114.

[51] S. Páll, A. Zhmurov, P. Bauer, M. Abraham, M. Lundborg, A. Gray, B. Hess, E. Lindahl, Heterogeneous parallelization and acceleration of molecular dynamics simulations in GROMACS, Journal of Chemical Physics 153 (13) (2020). doi:10.1063/5.0018516.

[52] Lindahl, Abraham, Hess, v. der Spoel, GROMACS 2020.7 Source code (2 2022). doi:10.5281/zenodo.5938877. URL `https://doi.org/10.5281/zenodo.5938877`

[53] Lindahl, Abraham, Hess, v. der Spoel, GROMACS 2021 Source code (1 2021). doi:10.5281/zenodo.4457626. URL `https://doi.org/10.5281/zenodo.4457626`

[54] M. Bernetti, G. Bussi, Pressure control using stochastic cell rescaling, The Journal of Chemical Physics 153 (11) (2020) 114107.

[55] G. Bussi, T. Zykova-Timan, M. Parrinello, Isothermal-isobaric molecular dynamics using stochastic velocity rescaling, Journal of Chemical Physics 130 (7) (2009). doi:10.1063/1.3073889.

[56] V. Corradi, E. Mendez-Villuendas, H. I. Ingólfsson, R.-X. Gu, I. Siuda, M. N. Melo, A. Moussatova, L. J. DeGagne, B. I. Sejdiu, G. Singh, others, Lipid–protein interactions are unique fingerprints for membrane proteins, ACS central science 4 (6) (2018) 709–717.

[57] S. Pandiyan, P. V. Parandekar, O. Prakash, T. K. Tsotsis, N. N. Nair, S. Basu, Controlling the sub-molecular motions to increase the glass transition temperature of polymers, Chemical Physics Letters 593 (2014). doi:10.1016/j.cplett.2013.12.076.

[58] E. A. Evans, R. Waugh, L. Melnik, Elastic area compressibility modulus of red cell membrane, Biophysical Journal 16 (6) (1976). doi:10.1016/S0006-3495(76)85713-X.

[59] W. Rawicz, K. C. Olbrich, T. McIntosh, D. Needham, E. A. Evans, Effect of chain length and unsaturation on elasticity of lipid bilayers, Biophysical Journal 79 (1) (2000). doi:10.1016/S0006-3495(00)76295-3.

[60] G. Saher, B. Brügger, C. Lappe-Siefke, W. Möbius, R.-i. Tozawa, M. C. Wehr, F. Wieland, S. Ishibashi, K.-A. Nave, High cholesterol level is essential for myelin membrane growth, Nature neuroscience 8 (4) (2005) 468–475.

[61] I. Bjorkhem, S. Meaney, Brain cholesterol: long secret life behind a barrier, Arteriosclerosis, thrombosis, and vascular biology 24 (5) (2004) 806–815.

[62] X. F. Jiang, K. Yang, X. Q. Yang, Y. F. Liu, Y. C. Cheng, X. Y. Chen, Y. Tu, Elastic modulus affects the growth and differentiation of neural stem cells, Neural Regeneration Research 10 (9) (2015). doi:10.4103/1673-5374.165527.

[63] L. Picas, F. Rico, S. Scheuring, Direct measurement of the mechanical properties of lipid phases in supported bilayers, Biophysical Journal 102 (1) (2012). doi:10.1016/j.bpj.2011.11.4001.

[64] O. Et-Thakafy, N. Delorme, C. Gaillard, C. Mériadec, F. Artzner, C. Lopez, F. Guyomarch, Mechanical Properties of Membranes Composed of Gel-Phase or Fluid-Phase Phospholipids Probed on Liposomes by Atomic Force Spectroscopy, Langmuir 33 (21) (2017). doi:10.1021/acs.langmuir.7b00363.

[65] N. M. Fonseka, F. T. Arce, H. S. Christie, C. A. Aspinwall, S. S. Saavedra, Nanomechanical Properties of Artificial Lipid Bilayers Composed of Fluid and Polymerizable Lipids, Langmuir 38 (1) (2022). doi:10.1021/acs.langmuir.1c02098.

[66] E. A. Evans, R. Waugh, Osmotic correction to elastic area compressibility measurements on red cell membrane, Biophysical Journal 20 (3) (1977). doi:10.1016/S0006-3495(77)85551-3.

[67] B. Daily, E. L. Elson, G. I. Zahalak, Cell poking. Determination of the elastic area compressibility modulus of the erythrocyte membrane, Biophysical Journal 45 (4) (1984). doi:10.1016/S0006-3495(84)84209-5.

[68] Z. Zhou, X. Li, Y. Liu, W. N. Hardy, S. Kleiven, Brain strain rate response: Addressing computational ambiguity and experimental data for model validation, Brain Multiphysics 4 (2023). doi:10.1016/j.brain.2023.100073.

[69] A. E. Davis, Mechanisms of traumatic brain injury: Biomechanical, structural and cellular considerations, Critical Care Nursing Quarterly 23 (3) (2000). doi:10.1097/00002727-200011000-00002.

[70] B. Morrison, H. L. Cater, C. D. Benham, L. E. Sundstrom, An in vitro model of traumatic brain injury utilising two-dimensional stretch of organotypic hippocampal slice cultures, Journal of Neuroscience Methods 150 (2) (2006). doi:10.1016/j.jneumeth.2005.06.014.

[71] A. C. Bain, D. F. Meaney, Tissue-level thresholds for axonal damage in an experimental model of central nervous system white matter injury, Journal of Biomechanical Engineering 122 (6) (2000). doi:10.1115/1.1324667.

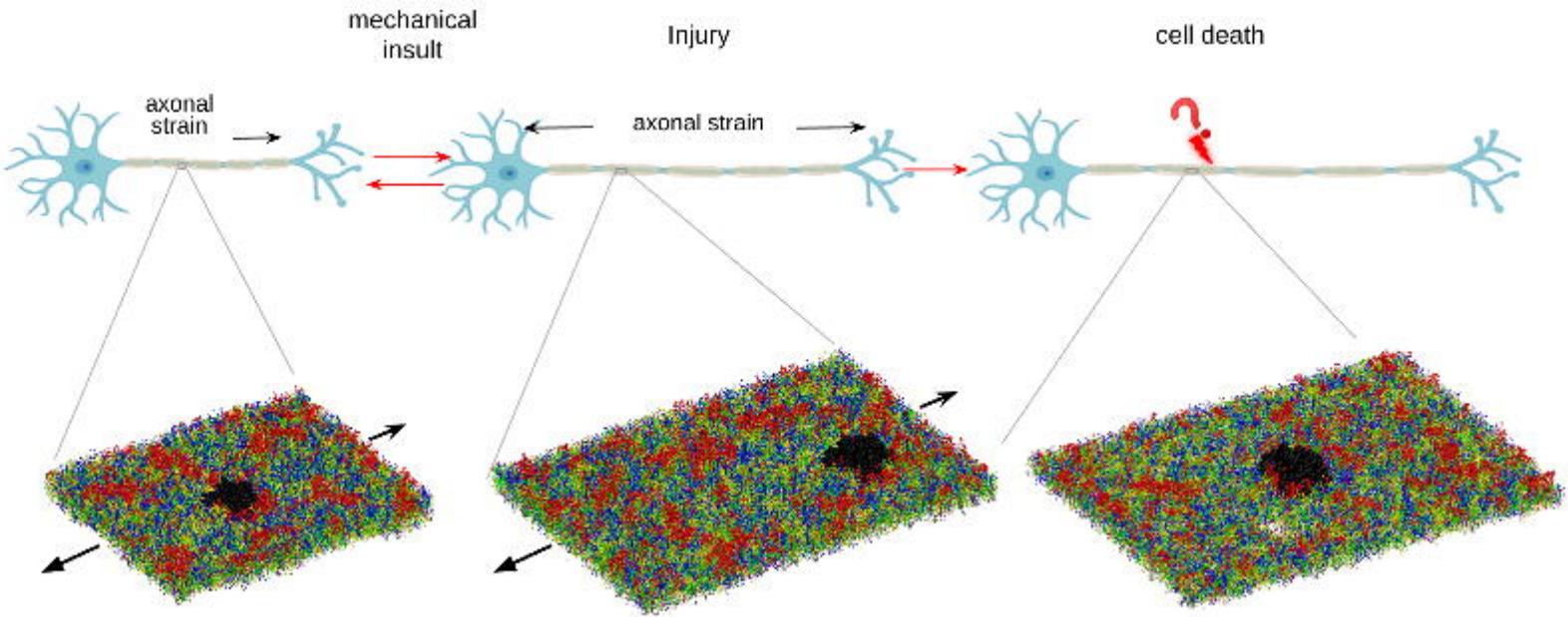
mechanical insult
Injury
cell death
axonal strain
axonal strain